INTERNATIONAL JOURNAL FOR NUMERICAL METHODS IN FLUIDS
Int. J. Numer. Meth. Fluids 2006; **50**:733–750
Published online 30 September 2005 in Wiley InterScience (www.interscience.wiley.com). DOI: 10.1002/fld.1077

An immersed boundary method for incompressible flows using volume of body function

Dartzi Pan*,†

Department of Aeronautics and Astronautics, National Cheng Kung University, Tainan, Taiwan, R.O.C

SUMMARY

A simple and effective immersed boundary method using volume of body (VOB) function is implemented on unstructured Cartesian meshes. The flow solver is a second-order accurate implicit pressure-correction method for the incompressible Navier–Stokes equations. The domain inside the immersed body is viewed as being occupied by the same fluid as outside with a prescribed divergence-free velocity field. Under this view a fluid–body interface is similar to a fluid–fluid interface encountered in the volume of fluid (VOF) method for the two-fluid flow problems. The body can thus be identified by the VOB function similar to the VOF function. In fluid–body interface cells the velocity is obtained by a volume-averaged mixture of body and fluid velocities. The pressure inside the immersed body satisfies the same pressure Poisson equation as outside. To enhance stability and convergence, multigrid methods are developed to solve the difference equations for both pressure and velocity. Various steady and unsteady flows with stationary and moving bodies are computed to validate and to demonstrate the capability of the current method. Copyright © 2005 John Wiley & Sons, Ltd.

KEY WORDS: immersed boundary method; implicit pressure-correction method; unstructured Cartesian meshes; volume of body

INTRODUCTION

Recently, numerical methods for solving incompressible flows on fixed Cartesian grids are gaining popularity for their relative ease in treating complex immersed bodies [1–8]. In immersed boundary method [1] the force applied by the elastic fibre to the fluid is computed and added to the fluid equations. In virtual boundary method [2, 3] the effect of solid body on the flow is modelled by a forcing term governed by a feedback loop that enforces the no-slip boundary condition at the fluid–solid interface. In these methods [1–3] the force term

*Correspondence to: Dartzi Pan, Department of Aeronautics and Astronautics, National Cheng Kung University, Tainan, Taiwan 70101, R.O.C.
†E-mail: dpan@mail.ncku.edu.tw

Contract/grant sponsor: National Science Council, Taiwan ROC; contract/grant numbers: NSC91-2212-E006-104, NSC92-2212-E006-105

Received 31 May 2004
Revised 13 July 2005
Accepted 17 July 2005

added to the flow field is spread over several grid cells using a delta-function-like distribution normal to the fluid–solid interface. In the direct-forcing methods [4, 5] the no-slip boundary condition at the fluid–solid interface is used as a condition to obtain directly the velocity around and inside the solid body without actually solving the fluid equations. The fictitious domain method [6] is a finite element method that enforces the fluid–body interface boundary condition in a weak form using Lagrange multipliers. The Lagrange multiplier can be viewed as a momentum-forcing term similar to the term added in the immersed boundary method. In Cartesian cut-cell method [7], the flow variables for the cut cells are solved based on the actual shape of the merged cut cells. In Reference [8], the solid body is viewed as being made of a material distinct from the surrounding fluid. The motion of the body is identified and tracked by a colour function. In the method implemented by Kajishima and Takiguchi [9], the volume fraction of solid is used to couple the fluid velocity and the solid velocity. This coupling is written as a forcing term in the momentum equation, which is implemented by a separate step in a fractional-step method.

Assuming that the motion of the immersed body is known in advance or can be computed by some structural equations, the differences among the above-mentioned methods lie in the different ways the no-slip boundary condition for the immersed bodies is enforced on a non-body-conformal Cartesian mesh. The cells surrounding and containing the fluid–body interface can be viewed as a transition region that connects the flow solution outside the body to the known velocity distribution inside the body. The problem can be further simplified by viewing the body interior as being occupied by same incompressible fluid as outside with a prescribed divergence-free velocity field. In this view a fluid–body interface is similar to a fluid–fluid interface encountered in the volume of fluid (VOF) method for the two-fluid flow problems. The body can thus be identified by the volume of body (VOB) function analogous to the VOF function. Since the body velocity is assumed incompressible, the pressure field inside the body obeys the same governing equation as the pressure outside. This is the basic idea we used to develop a simple immersed boundary method using the VOB function. This idea is similar to the one implemented by Xiao [8] and the one by Kajishima and Takiguchi [9]. However, the actual implementation of the concept is different among these methods.

In this work an implicit fractional step pressure-correction method is first developed to solve the incompressible Navier–Stokes equations on unstructured Cartesian meshes. The method is second-order accurate both in time and in space. The VOB function is then used as a natural parameter that relates the flow velocity outside the body to the known velocity distribution inside the body. For interface cells containing the fluid–body interface, the velocity is computed by the volume average of the velocity of the two ‘fluids’. In the advection–diffusion step of the fractional-step method, the VOB-coupled equations for velocity are implicitly integrated using the technique of sub-iteration. In the pressure-correction step, the pressure-correction Poisson equation applies to the entire computational domain regardless of the cell type. The capability of local refinement on unstructured Cartesian grid is advantageous to enhance the resolution around the fluid–solid interface. For stable and fast convergence, implicit multigrid methods are developed to solve the difference equations for both pressure and velocity. Note that the current implementation for the coupling between fluid and body velocity is different form the procedure in References [8, 9], where an explicit fractional step is performed for the velocity coupling. To test the validity of the current method, the steady and unsteady flows in a driven cavity and over a circular cylinder are computed and compared with the published data. Finally, the wake flow of an impulsively started cylinder and a cylinder oscillating inline

with the free stream are computed to demonstrate the capability of the present method to treat moving bodies.

IMPLICIT PRESSURE-CORRECTION METHOD

The incompressible Navier–Stokes equations are

$$\begin{gathered}\nabla \cdot \mathbf{v} = 0 \\ \frac{\partial}{\partial t}\int_{\mathrm{CV}} \mathbf{v}\,\mathrm{d}V + \oint_{\mathrm{CS}} \mathbf{v}\mathbf{v}\cdot\mathrm{d}\mathbf{S} - \oint_{\mathrm{CS}} \frac{1}{Re}\nabla\mathbf{v}\cdot\mathrm{d}\mathbf{S} + \oint_{\mathrm{CS}} P\,\mathrm{d}\mathbf{S} = 0\end{gathered} \tag{1}$$

where $\mathbf{v}$ and P are Cartesian velocity vector and pressure; Re is Reynolds number; CV is the control volume considered and CS is the boundary surface of CV. Applying the Divergence theorem and adapting the backward time differencing scheme, the momentum equation with the pressure fixed at time level n can be written as

$$\left(\frac{c_1\mathbf{v}^* - c_2\mathbf{v}^n + c_3\mathbf{v}^{n-1}}{\Delta t} + \mathbf{R}^* + \nabla P^n\right)\Delta V = 0 \tag{2}$$

where the superscript '*' represents the intermediate state; 'n' represents the current time level; ΔV is the volume of the considered cell; Δt is the time increment; $\mathbf{R}$ represents the volume integral of convection and the viscous fluxes. The constants are $c_1 = 1.5$, $c_2 = 2$ and $c_3 = 0.5$ for the second-order accurate backward difference scheme, and $c_1 = 1$, $c_2 = 1$ and $c_3 = 0$ for the first-order Euler implicit scheme. The intermediate velocity $\mathbf{v}^*$ generally does not satisfy the divergence-free condition. The velocity and the pressure are corrected by the following steps:

$$\begin{aligned}\mathbf{v}^{n+1} &= \mathbf{v}^* - \Delta t\nabla\phi^n \\ P^{n+1} &= P^n + \phi^n\end{aligned} \tag{3}$$

where ϕ is the pressure correction. By requiring $\mathbf{v}^{n+1}$ be divergence free, we obtain the Poisson equation for the pressure correction:

$$\nabla^2\phi^n - \frac{\nabla\cdot\mathbf{v}^*}{\Delta t} = 0 \tag{4}$$

Equations (2)–(4) constitute the implicit fractional step pressure-correction method used in this work.

FINITE VOLUME DISCRETIZATION

A cell-centred finite volume method on unstructured Cartesian grid is developed in this work. The flow variables $\mathbf{v}$ and P are stored at the centre of the cell volume. The flow states at a cell vertex are obtained by averaging the surrounding centre values with the weighting constant proportional to the inverse of the distance to the particular centre. The variable gradients at

the cell centre are obtained by differencing the vertex values of the particular cell. The left and right variable states at a cell-face centre are linearly reconstructed from the immediate centre values using the estimated gradient information. The mean variable states at the cell-face centres are then obtained by a simple average of the face values:

$$\mathbf{v}_{\mathrm{f}}^{\mathrm{M}} = 0.5(\mathbf{v}_{\mathrm{f}}^{\mathrm{L}} + \mathbf{v}_{\mathrm{f}}^{\mathrm{R}}), \quad P_{\mathrm{f}}^{\mathrm{M}} = 0.5(P_{\mathrm{f}}^{\mathrm{L}} + P_{\mathrm{f}}^{\mathrm{R}}) \tag{5}$$

where the sub-script f represents the face index; the superscripts M, L and R represent the mean, left and right states of face f. The convection flux $\mathbf{R}_{\mathrm{conv}}$ is computed as

$$\mathbf{R}_{\mathrm{conv}} = \frac{1}{\Delta V} \sum_{\mathrm{CS}} \begin{bmatrix} u \\ v \end{bmatrix}_{\mathrm{L/R}} \mathbf{v}_{\mathrm{f}}^{\mathrm{M}} \cdot \hat{n} \Delta S \tag{6}$$

where ΔS is the face area; $\hat{n}$ is the unit surface normal pointing outward; and the summation operator is done over all surfaces of the cell. The sub-script L/R represents the velocity upwinding:

$$(\bullet)_{\mathrm{L//R}} = \begin{cases} (\bullet)^{\mathrm{L}} & \text{if } \mathbf{v}_{\mathrm{f}}^{\mathrm{M}} \cdot \hat{n} > 0 \\ (\bullet)^{\mathrm{R}} & \text{if } \mathbf{v}_{\mathrm{f}}^{\mathrm{M}} \cdot \hat{n} \leqslant 0 \end{cases} \tag{7}$$

The pressure gradient at the cell centre is computed as

$$\boldsymbol{\nabla} P = \frac{1}{\Delta V} \sum_{\mathrm{CS}} P_{\mathrm{f}}^{\mathrm{M}} \hat{n} \Delta \mathbf{S} \tag{8}$$

The viscous fluxes $\mathbf{R}_{\mathrm{vis}}$ are computed as

$$\mathbf{R}_{\mathrm{vis}} = \frac{1}{Re \Delta V} \sum_{\mathrm{CS}} \begin{bmatrix} \boldsymbol{\nabla} u \\ \boldsymbol{\nabla} v \end{bmatrix} \cdot \hat{n} \Delta S \tag{9}$$

where u and v are the Cartesian velocity components. The velocity gradients at the cell-face centres are obtained by differencing the neighbouring cell-centre values. On a regular Cartesian grid, formulations (6)–(9) are second-order accurate spatial difference schemes for inviscid and viscous flux terms in Equation (2).

FACE-NORMAL VELOCITY

To compute the divergence of velocity, a face-normal velocity U_{f} is defined independently for each cell face, which is different from the cell-centre velocity. Specifically, for a cell face f with surface unit normal $\hat{n}$, the intermediate state of the face-normal velocity is defined as

$$U_{\mathrm{f}}^{*} = \mathbf{v}_{\mathrm{f}}^{\mathrm{M}} \cdot \hat{n} - \mathrm{cdisp} \frac{\Delta t}{\Delta \ell} (P_{\mathrm{f}}^{\mathrm{R}} - P_{\mathrm{f}}^{\mathrm{L}}) \hat{e} \cdot \hat{n} \tag{10}$$

where $\Delta\ell$ is the distance between the right and the left neighbouring cell centres; $\hat{e}$ is the Cartesian unit vector normal to the face; cdisp is an input constant for the pressure dissipation. The divergence of the intermediate velocity for a particular cell is computed as

$$\nabla \cdot \mathbf{v}^* = \frac{1}{\Delta V} \sum_{\mathrm{CS}} (U_{\mathrm{f}}^* \Delta S)$$

$$= \frac{1}{\Delta V} \sum_{\mathrm{CS}} \mathbf{v}_{\mathrm{f}}^{\mathrm{M}} \cdot \hat{n} \Delta S - \frac{\mathrm{cdisp} \Delta t}{\Delta V} \sum_{\mathrm{CS}} \frac{P_{\mathrm{f}}^{\mathrm{R}} - P_{\mathrm{f}}^{\mathrm{L}}}{\Delta \ell} \hat{e} \cdot \hat{n} \Delta S \tag{11}$$

The last term on the right-hand side of Equation (11) is a background dissipation term based on the pressure field. On a regular Cartesian grid it can be shown that this dissipation is proportional to $\mathrm{cdisp}(a\Delta x^2(\partial^4 P/\partial x^4) + b\Delta y^2(\partial^4 P/\partial y^4))$ where a and b are some constants. It has similar effects as the widely used momentum interpolation method [10]. Note that in Equation (10) the dissipation term is written in a simple form suitable for unstructured meshes.

PRESSURE-CORRECTION POISSON EQUATION

The intermediate face-normal velocity is corrected similarly as the cell-centre velocities by

$$U_{\mathrm{f}}^{n+1} = U_{\mathrm{f}}^* - \Delta t (\nabla \phi^n)_{\mathrm{f}} \cdot \hat{n} \tag{12}$$

where the gradient of pressure correction is computed at the cell-face centre. By demanding U_{f}^{n+1} be divergence free, a discrete Poisson equation for the pressure correction is constructed as

$$\frac{1}{\Delta V} \sum_{\mathrm{CS}} (\nabla \phi^n)_{\mathrm{f}} \cdot \hat{n} \Delta S - \frac{1}{\Delta t \Delta V} \sum_{\mathrm{CS}} U_{\mathrm{f}}^* \Delta S = 0 \tag{13}$$

Equation (13) is a compact discretization of Equation (4). It is used to compute the pressure correction ϕ^n at the cell centres, which in turn determines the cell-centre pressure and velocity at the new time level $n+1$ in Equation (3).

It should be mentioned that in References [5, 7] the desired pressure–velocity coupling is achieved by Equations (12) and (13) without the explicit addition of pressure dissipation in Equation (10). In this work we kept the dissipation term in Equation (10) as an extra means to control the possible pressure oscillation around the body surfaces. It should also be noted that in References [5, 7] the divergence-free $U_{\mathrm{f}}^{n+1}$is used to replace the term $\mathbf{v}_{\mathrm{f}}^{\mathrm{M}} \cdot \hat{n}$ in Equations (6) and (7) to compute the convection fluxes in the next time step. We chose not to do so because U_{f}^{n+1} depends explicitly on the chosen Δt.

TREATMENT OF IMMERSED BODY

The position and the velocity $\mathbf{v}_{\mathrm{B}}$ of the immersed bodies are assumed known from some appropriate governing equations. For the forced body motion examined in this work, we use

a level set function ϕ_L defined on the cell vertices to track the location of the immersed bodies. We chose ϕ_L to be a signed distance function whose absolute value equals the shortest distance to the body surface. It is defined $\phi_L > 0$ outside the body, $\phi_L < 0$ inside, and $\phi_L = 0$ on the body surface. With ϕ_L known, the volume fraction occupied by the immersed body in a cell, or the VOB function ϕ_B, can be computed easily. The VOB function is used to identify the body cells ($\phi_B = 1$), the fluid cells ($\phi_B = 0$) and the interface cells ($0 < \phi_B < 1$). For convenience, the body surface is represented by the contour of $\phi_B = 0.5$ or $\phi_L = 0$. Since the velocity inside the body surface is known, we modify Equation (2) to

$$(1-\phi_B)\Delta V\left(\frac{c_1\mathbf{v}^* - c_2\mathbf{v}^n + c_3\mathbf{v}^{n-1}}{\Delta t} + \mathbf{R}^* + \nabla P^n\right) + \phi_B \Delta V\left(\frac{c_1\mathbf{v}^* - c_1\mathbf{v}_B^{n+1}}{\Delta t}\right) = 0 \qquad (14)$$

Equation (14) recovers Equation (2) for fluid cells, and it yields $\mathbf{v}^* = \mathbf{v}_B^{n+1}$ for body cells. As for interface cells, the solution of Equation (14) is a volume-averaged mixture of the body velocity and the velocity computed by the flux conservation. This volume averaging is a simple and effective treatment to connect the flow solution in fluid cells to the boundary condition ($\mathbf{v}_B^{n+1}$) in body cells. Note that the VOB-averaged interface variables satisfy Equation (14) instead of Equation (2). Thus, interface cells should be excluded from the residual computation. Equation (14) is different from the velocity-coupling step in References [8, 9].

Note that the boundary contour of the domain occupied by all body cells with $\phi_B = 1$ is a closed stair-step-like zigzag contour. The volume averaging of velocity in interface cells has the effect of smoothening the stair-step representation of the body surface. The true location of the body surface is embedded in the interface cells with an uncertainty of one cell size. In this work the capability of local refinement on unstructured Cartesian grid is developed, which is useful to enhance the grid resolution around the body surface.

In essence, the domain inside the body surface is viewed as being occupied by same fluid as outside with a prescribed incompressible velocity distribution. In this view, there is no property jump across the body surface, and the pressure inside the body surface obeys the same governing equation as outside. Thus, the Poisson equation for pressure correction, Equation (13), is used for the entire computational domain without distinguishing the cell type. When the given $\mathbf{v}_B^{n+1}$ is divergence free, the source term of Equation (13) is zero automatically. The pressure inside the body is of no physical meaning. The elliptical nature of the Poisson equation ensures that the pressure field inside the body adjusts itself according to the pressure field outside.

To compute the forces acting on the body, the surface integral of the pressure and viscous stresses over the closed body surface is transformed into a volume integral using the Gauss theorem. Specifically, the total force acting on the immersed body is obtained by

$$\mathbf{f}_{\text{Body}} = \sum_{\text{cell}} \phi_B \Delta V\left(-\nabla P + \frac{1}{Re}\nabla^2\mathbf{v}\right) \qquad (15)$$

Note that the surface normal direction is automatically determined by the distribution of VOB function ϕ_B.

IMPLICIT INTEGRATION OF ADVECTION–DIFFUSION STEP

Applying the Newton's method to Equation (14) and writing it in delta-law form, the implicit time integration equation of intermediate velocity can be written as

$$\left(\frac{c_1\Delta V}{\Delta t}+(1-\phi_B)\Delta V\frac{\partial \mathbf{R}}{\partial \mathbf{v}}\right)(\mathbf{v}^{s+1}-\mathbf{v}^s)$$
$$=-\left\{(1-\phi_B)\Delta V\left(\frac{c_1\mathbf{v}^s-c_2\mathbf{v}^n+c_3\mathbf{v}^{n-1}}{\Delta t}+\mathbf{R}^s+\nabla P^n\right)+\phi_B\Delta V\left(\frac{c_1\mathbf{v}^s-c_1\mathbf{v}_B^{n+1}}{\Delta t}\right)\right\}$$
$$=\mathrm{Res}^s \tag{16}$$

where the superscript s is the index for sub-iteration, and Res^s is the right-hand residual. Equation (16) can be further represented by

$$[\mathrm{LHS}](\mathbf{v}^{s+1}-\mathbf{v}^s)=-\{\mathrm{RHS}(\mathbf{v}^s)-\mathrm{Source}\}$$
$$=\mathrm{Res}^s \tag{17}$$

where $-$(RHS) is the right-hand side operator involving only the current velocity vector $\mathbf{v}^s$; 'Source' represents all terms involving known states of pressure P^n, velocity $\mathbf{v}^n$, $\mathbf{v}^{n-1}$ and $\mathbf{v}_B^{n+1}$ in the residual; LHS is the Jacobian matrix of RHS. When the sub-iteration in s converges, the solution is $\mathbf{v}^{s+1}=\mathbf{v}^*$, satisfying the time-accurate Equation (14). Note that term 'Source' is constant during the sub-iteration. In operator LHS, the first-order upwind scheme is used for the convection flux Jacobian and the compact difference operator is used for the viscous flux Jacobian. With these simplifications, the stencil of LHS extends only to the neighbouring cell centres while the right-hand side operators are kept second-order accurate.

Splitting LHS into the sum of a diagonal part D, a lower triangular part L and an upper triangular part U, a two-step approximate LU factorization method is used to invert Equation (17) approximately as

$$\omega U\Delta\mathbf{v}^{s-1}+(D+\omega L)\Delta\mathbf{v}^{s*}=\omega(2-\omega)\mathrm{Res}^s$$
$$\omega L\Delta\mathbf{v}^{s*}+(D+\omega U)\Delta\mathbf{v}^s=\omega(2-\omega)\mathrm{Res}^s \tag{18}$$
$$\mathbf{v}^{s+1}=\mathbf{v}^s+\Delta\mathbf{v}^s$$

where ω is a relaxation parameter, and here we take $0.9\leqslant\omega\leqslant1$. The initial conditions are $\mathbf{v}^s=\mathbf{v}^n$ and $\Delta\mathbf{v}^{s-1}=0$ for $s=1$.

MULTIGRID METHOD FOR VELOCITY

It is our experience that the convergence rate of Equation (18) will deteriorate for highly refined grids. Thus, to accelerate the convergence, a V-cycle multigrid method is developed

on unstructured Cartesian grid for Equations (17) and (18). An unstructured Cartesian grid with local refinement is generated from an initial cell (parent cell) that covers the entire flow field. This initial cell is recursively sub-divided into 4 identical children cells (8 children cells in 3D) until sufficient spatial resolution around the body surface is reached. The tree structure among the parent cells and their children cells provides a natural sequence of grid coarsening from fine to coarse grids. For simplicity, we describe below only a two-level multigrid cycle.

On the coarse grid, the equation to be solved is

$$\begin{aligned} &-\{\mathrm{RHS}^{\mathrm{C}}(\mathbf{v}^{\mathrm{C}}) - \mathrm{Source}^{\mathrm{C}}\} = 0 \\ &\mathrm{Source}^{\mathrm{C}} = [\mathrm{RHS}^{\mathrm{C}}(J_{\mathrm{F}}^{\mathrm{C}}\mathbf{v}^{\mathrm{F}}) + I_{\mathrm{F}}^{\mathrm{C}}\mathrm{Res}^{\mathrm{F}}] \end{aligned} \tag{19}$$

where the super- and the sub-script F and C represents the fine grid and the coarse grid variables or operators, respectively. The injection operator $J_{\mathrm{F}}^{\mathrm{C}}$ for velocity conserves $\mathbf{v}\Delta V$. The injection operator $I_{\mathrm{F}}^{\mathrm{C}}$ for residual vector conserves the surface integrals of convection and viscous fluxes. The operator $\mathrm{RHS}^{\mathrm{C}}$ on the coarse grid is theoretically equivalent to the operator RHS in Equation (17) on the fine grid. But simplification is achieved by using only first-order upwind difference for the convection fluxes on coarse grids of all levels. Note that the constant 'Source' term in Equation (17) on the finer grid is not present in the coarse grid equation. Equation (19) has exactly the same form as the right-hand side of Equation (17). Applying again the Newton's method to Equation (19), an implicit integration equation equivalent to Equation (17) can be constructed on the coarse grid, and then solved for $\mathbf{v}^{\mathrm{C}}$ by the same relaxation method as described by Equation (18).

When Equation (19) has been resolved for $\mathbf{v}^{\mathrm{C}}$, the prolongation operator $J_{\mathrm{C}}^{\mathrm{F}}$ transfers the estimated correction from the coarse grid back to the finer grid by

$$\mathbf{v}^{\mathrm{F},s+1} = \mathbf{v}^{\mathrm{F}} + J_{\mathrm{C}}^{\mathrm{F}}(\mathbf{v}^{\mathrm{C}} - J_{\mathrm{F}}^{\mathrm{C}}\mathbf{v}^{F}) \tag{20}$$

where $J_{\mathrm{F}}^{\mathrm{C}}\mathbf{v}^{\mathrm{F}}$ is the initial velocity vector injected from the fine grid; and $J_{\mathrm{C}}^{\mathrm{F}}$ is the prolongation operator. In this work a simple prolongation that assumes a constant distribution in the parent cell is used. Specifically, a parent (coarse) cell transfers the calculated correction evenly to all its children (fine) cells. On the finest grid (terminal grid), the body cells with $\phi_{\mathrm{B}} = 1$ are excluded from the prolongation procedure.

IMPLICIT RELAXATION AND MULTIGRID METHOD FOR PRESSURE CORRECTION

Applying the Newton's method to Equation (13), the implicit relaxation method can be written as

$$\begin{aligned} \nabla^2 \Delta V(\phi^{s+1} - \phi^s) &= -\left\{ \sum_{\mathrm{CS}} (\boldsymbol{\nabla}\phi^s)_{\mathrm{f}} \cdot \hat{n}\Delta S - \frac{1}{\Delta t} \sum_{\mathrm{CS}} U_{\mathrm{f}}^* \Delta S \right\} \\ &= \mathrm{Res}_{\phi}^{s} \end{aligned} \tag{21}$$

where s is the index for sub-iteration. When the iteration in s converges, the solution is $\phi^{s+1} = \phi^n$, which satisfies the Poisson equation, Equation (13). The left-hand side operator is a compact Laplacian operator whose stencil extends only to the neighbouring cell centres. Equation (21) can be further represented by

$$[\mathrm{LHS}_\phi](\phi^{s+1} - \phi^s) = -\{\mathrm{RHS}(\phi^s) - \mathrm{Source}_\phi\}$$
$$= \mathrm{Res}_\phi^s \tag{22}$$

where the term Source_ϕ is related to the divergence of velocity field. Note that this equation is in the same form as Equation (17). Hence, similar to the method described above, an implicit relaxation method and a V-cycle multigrid method are developed to solve Equation (22). The initial conditions are $\phi^s = 0$ and $\Delta\phi^{s-1/2} = 0$ for $s = 1$.

ORDER ANALYSES FOR FRACTIONAL-STEP METHOD

In the following sections, we present some validation results for the current methodology. All computations are done on a personal computer with single precision. The analytical solutions of decaying vortices [11] are used for order analyses:

$$\begin{aligned} u(x, y, t) &= -\cos(\pi x)\sin(\pi y)\mathrm{e}^{-2\pi^2 t/Re} \\ v(x, y, t) &= \sin(\pi x)\cos(\pi y)\mathrm{e}^{-2\pi^2 t/Re} \\ P(x, y, t) &= -\frac{\cos(2\pi x) + \cos(2\pi y)}{4}\,\mathrm{e}^{-4\pi^2 t/Re} \end{aligned} \tag{23}$$

Here we take $-0.5 \leqslant x,\ y \leqslant 0.5$ and $Re = 10$. Exact solutions are used as initial and boundary conditions. The implicit backward differencing scheme is used for time integration. To start the time integration at $n = 0$, the second-order trapezoidal rule is used as a starter such that no initial condition at $n = -1$ is required.

For time accuracy test, the regular Cartesian grid spacing is fixed at $\Delta x = 0.0078125$ and the time increment is varied among $\Delta t = 0.1,\ 0.05,\ 0.025$, and 0.0125. The solution at $t = 0.3$ is compared with the exact solution, and the maximum error in u is plotted in Figure 1(a). To show the spatial accuracy, the time step is fixed at $\Delta t = 0.003$ and the grid spacing is varied among $\Delta x = 1/128,\ 1/64$ and $1/32$. The solutions at $t = 0.3$ are compared with the exact solution, and the maximum error in u is plotted in Figure 1(b). It is seen that the current method is a second-order method both in time and in space.

DRIVEN CAVITY FLOWS

The numerical solutions of driven cavity flows obtained by Ghia *et al.* [12] are used to test the steady state computation of the present method. A Cartesian grid of size 128×128 is used to discretize a square cavity of unit length in size. The upper wall is moving to the right at unit speed. For the case of $Re = 3200$, the time step is set to $\Delta t = 0.15$ and artificial dissipation is

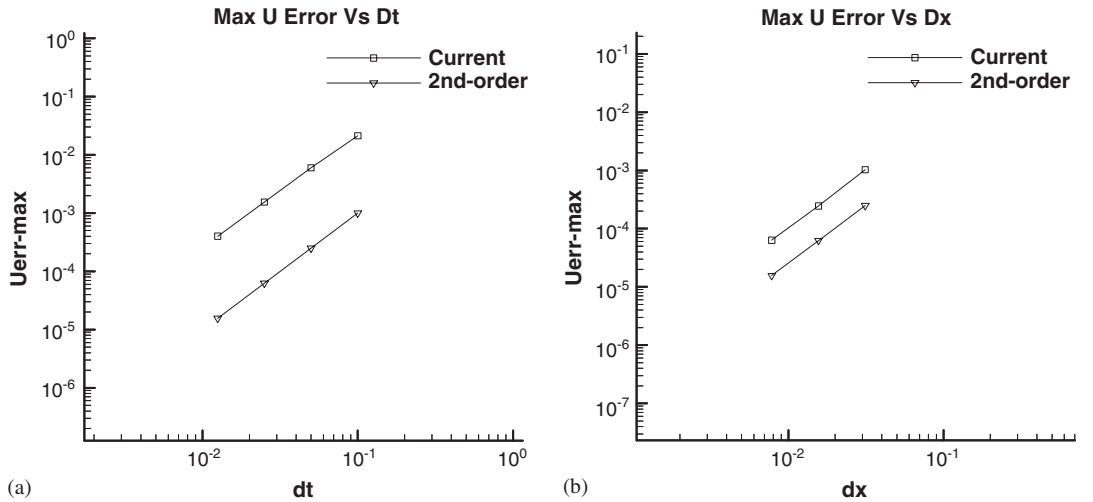

Figure 1. Decaying vortices test, $Re = 10$: (a) time accuracy; and (b) spatial accuracy.

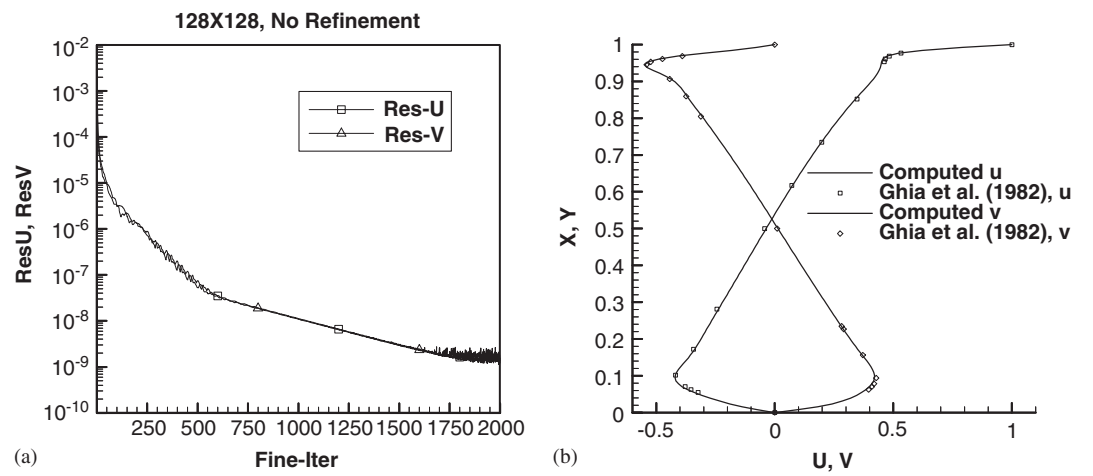

Figure 2. Driven cavity, $Re = 3200$: (a) convergence history of the maximum norm of steady state residual; and (b) $u(y)$ and $v(x)$ along centrelines, lines: computed, symbols: Ghia *et al.* [12].

set to cdisp = 0.1. The maximum CFL number in the computation is about 15. The maximum norm of the steady state residual, or the terms in Equation (14) without involving Δt, dropped more than four orders of magnitude to 1×10^{-8} in 1100 steps of fine grid variable update and reached machine zero in about 2000 steps, as shown in Figure 2(a). The velocity component in x direction along the vertical centreline, $u(y)$, and the velocity component in y direction

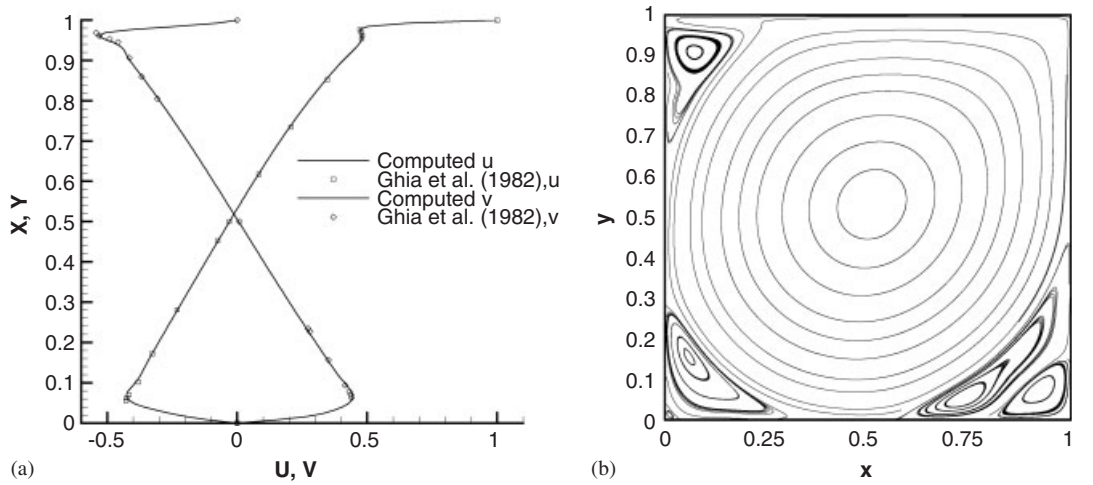

Figure 3. Driven cavity, $Re = 10\,000$: (a) $u(y)$ and $v(x)$ along centrelines, lines: computed, symbols: Ghia *et al.* [12]; and (b) streamlines.

along the horizontal centreline, $v(x)$, are plotted in Figure 2(b). The comparisons with the results obtained by Ghia *et al.* [12] who also used 128×128 grid are very good. For the case of $Re = 10\,000$, the time step is set to $\Delta t = 0.1$ and artificial dissipation is set to cdisp $= 0.2$. The maximum CFL number in the computation is about 10. In this case the convergence slows down considerably. The maximum norm of the steady state residual dropped more than four orders of magnitude to 1×10^{-8} in 5000 steps and reached machine zero in about 8000 steps. Figure 3(a) shows the computed velocity profiles $u(y)$ and $v(x)$ along vertical and horizontal centrelines, respectively. The comparisons with Ghia *et al.* [12] who used a 256×256 grid are satisfactory. The computed streamlines for $Re = 10\,000$ case are plotted in Figure 3(b), showing one primary vortex in the centre, one secondary vortex (TL1) on the top side of the left wall, one secondary vortex (BR1) and one tertiary vortex (BR2) in the bottom right corner, one secondary vortex (BL1) and one tertiary vortex (BL2) in the bottom left corner. Note that the vortex BL2 has a size of two to three cells only. In Reference [12] another quaternary vortex BR3 was shown on the bottom right corner. In this work the vortex BR3 was not captured because only a 128×128 was used.

FLOWS OVER A STATIONARY CIRCULAR CYLINDER

To test the model for the immersed bodies, the steady and unsteady flows over a circular cylinder of unit diameter are computed on unstructured Cartesian grids. The grid is refined around the cylinder surface such that there are about 384 interface cells. The cylinder volume computed by summing up $\phi_B \Delta V$ is 0.7853632, which is about 0.01% less than the true value of 0.25π. The outer boundaries are 30 diameters away from the origin. The uniform flow condition is set to the inflow boundary and the two boundaries in y. The downstream

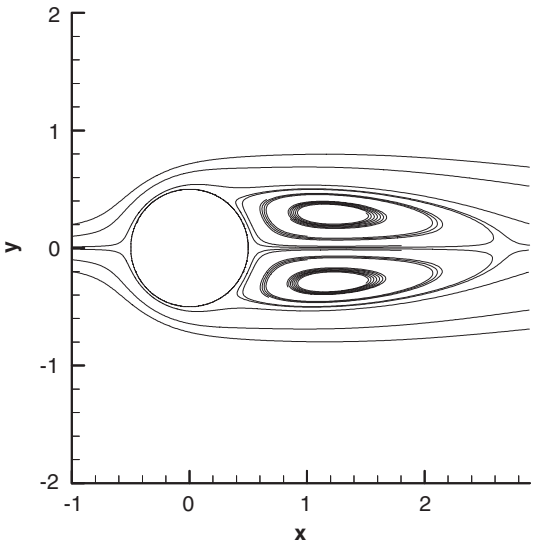

Figure 4. Flows over a stationary circular cylinder, $Re = 40$, streamlines.

boundary follows the upwind differenced equation of $(\partial \mathbf{v}/\partial t) + U_n(\partial \mathbf{v}/\partial x) = 0$, where U_n is the computed normal outflow velocity at the boundary.

For the steady case of $Re = 40$, the Euler implicit method is used with the maximum CFL number around 25. The infinity norm of the steady state residual for $\phi_B = 0$ cells, or the terms in Equation (14) without involving Δt, dropped four orders of magnitude in 500 steps. The computed streamlines are plotted in Figure 4. For convenience, the contour of $\phi_L = 0$ is displayed as the cylinder wall. The flow is steady with a separation bubble behind the cylinder. The streamlines around the cylinder are smooth, indicating the effects of the interface cells in smoothening the zigzag representation of the cylinder surface. Figure 5(a) shows the computed pressure contours. Note that the pressure inside the cylinder adjusts itself automatically to the pressure field outside. The pressure contours intersect the cylinder wall in a nearly orthogonal manner. To examine the surface pressure distribution, the pressure coefficient at the intersection of the cylinder surface and the grid lines is interpolated using the surrounding centre values and plotted in Figure 5(b). The data measured from Reference [13] are also included for comparison. The two results generally agree with each other very well. The current computation predicted a slightly lower surface pressure distribution on the leeward surface. Note that the computed surface pressure has only very minor wiggles around the shoulder region. It would show zigzag oscillation if the dissipation term in Equation (10) was turned off. Here, a constant cdisp $= 0.1$ is used to minimize such oscillations.

Table I lists the computed lift (Cl) and drag (Cd) coefficients using Equation (15) and the wake length (Lw) normalized by the diameter (d). The computed results for the case of $Re = 20$ are also listed. The comparison with the work of others is generally satisfactory.

For the unsteady case of $Re = 200$, the second-order backward difference scheme is used. The time increment is chosen such that the expected vortex shedding cycle takes about 50

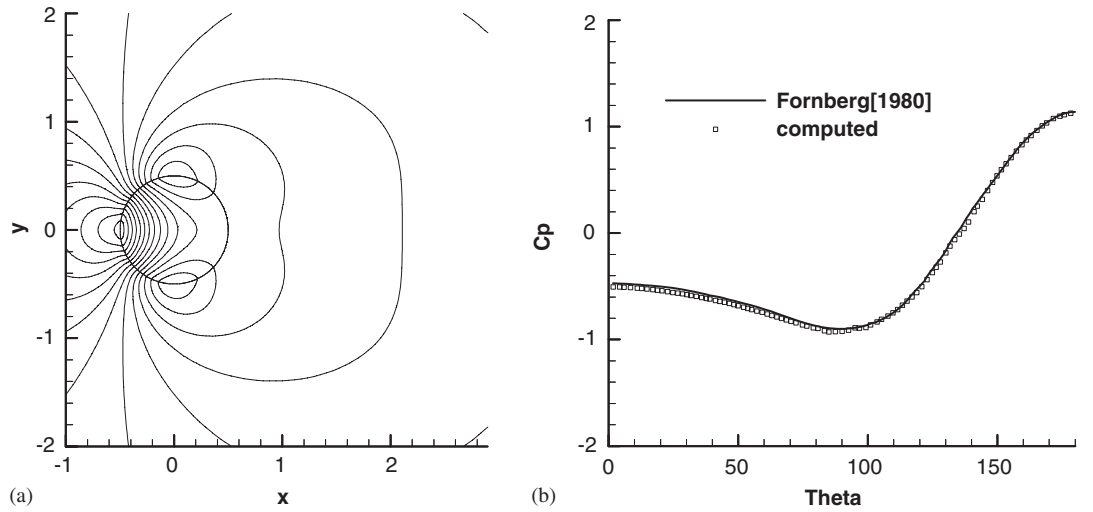

Figure 5. Flows over a stationary circular cylinder, $Re = 40$: (a) Cp contours; and (b) surface Cp distribution, symbol: computed, line: data taken from Fornberg [13].

Table I. Simulation results for flows over a circular cylinder.

Methods	*Re*	Cd	Lw/d	Cl	*St*
Current	20	2.01	0.85	8×10^{-6}	
Fornberg [13]	20	2.00	0.91		
Ye *et al.* [7]	20	2.03	0.92		
Current	40	1.50	2.13	3×10^{-6}	
Fornberg [13]	40	1.50	2.24		
Ye *et al.* [7]	40	1.52	2.27		
Current	200	1.27 ± 0.04		± 0.60	0.20
Kiris and Kwak [14]	200	1.27 ± 0.04		± 0.67	0.184

time steps to complete. The instantaneous streamlines at certain instant in the periodic vortex shedding process are plotted in Figure 6(a). Figure 6(b) shows the vorticity contours. The unsteady vortex shedding behind the cylinder is clearly seen. The computed aerodynamic coefficients and the Strouhal number (St) based on the lift coefficient are listed in Table I. The comparison with the work of others is generally satisfactory. Note that in Reference [14], various computational and experimental results for $Re = 200$ case were listed. The listed Cl ranged from ± 0.5 to ± 0.7; Cd ranged from 1.17 ± 0.0005 to 1.58 ± 0.0035 and St ranged from 0.16 to 0.227.

IMPULSIVELY STARTED CYLINDER

To test the applicability of the present method to the flow field with moving body, the case of an impulsively started cylinder was computed and compared with the experimental data by

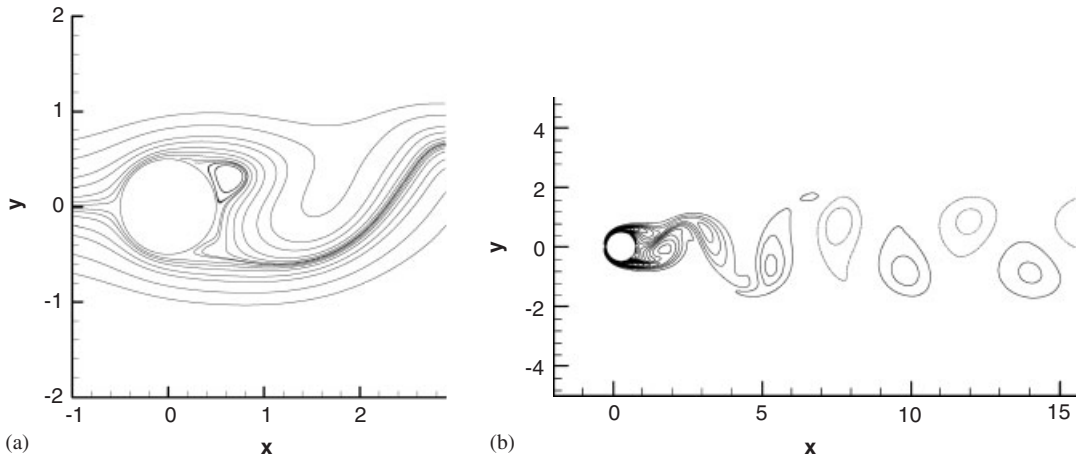

Figure 6. Flow over a stationary cylinder, $Re = 200$: (a) instantaneous streamlines; and (b) vorticity contours.

Bouard and Coutanceau [15]. The cylinder was initially at rest and was suddenly moved to the left at a constant speed. The Reynolds number based on the cylinder diameter D and cylinder speed U_{cyl} is 550. The mesh is clustered along the path of the cylinder movement such that there are always about 312 interface cells around the cylinder. During the computation of 600 time steps, the cylinder was moved a distance of 3 diameters from its initial position. Figure 7 shows the time-dependent development of velocity along the symmetry axis in the wake. In this figure the velocity u was measured relative to the moving cylinder and normalized by the cylinder speed U_{cyl}. The distance x/D along the symmetry axis was referenced relative to the cylinder centre. The symbols in Figure 7 are measured manually from the experimental points in Bouard and Coutanceau [15], while the lines are from our computation. Different symbols correspond to different time $t_s = tU_{\text{cyl}}/D$ with an increment of 0.5, starting from $t_s = 0.5$. The agreement between computation and experiment is generally satisfactory. Figure 8 shows the computed instantaneous streamlines at $t_s = 3.0$. A pair of isolated secondary vortex between the shoulder and the rear stagnation can be clearly seen. This is in good agreement with the experimental observation of Bouard and Coutanceau [15]. This example basically has validated the capability of the present method to treat moving bodies in the flow field.

FLOW OVER AN OSCILLATING CYLINDER

This computation was performed at $Re = 200$ with the cylinder oscillating in parallel to the free stream velocity. The cylinder was forced to oscillate at a frequency $f_e = 1.5St$, that is, 1.5 times the Strouhal (St) number for the vortex shedding over a stationary cylinder. The centre of the cylinder moves along the x-axis harmonically like $x_c = A\sin[2\pi f_e(t - t_s) + 0.5\pi]$ with an amplitude $A = 0.24d$ and t_s is the time the oscillation starts. The velocity of the cylinder is

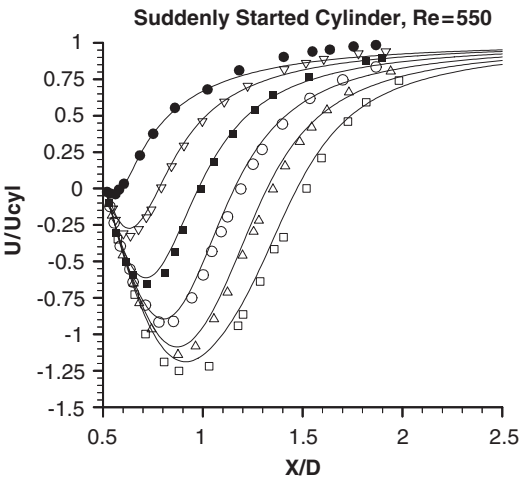

Figure 7. Velocity u along symmetry axis in the wake of an impulsively started cylinder, $U_{\text{cyl}}D/\nu = 550$, Symbols: experimental data of Bouard and Coutanceau [15] at different time $t_s = tU_{\text{cyl}}/D$ with an increment of 0.5, starting from $t_s = 0.5$ (solid circle), lines: computed.

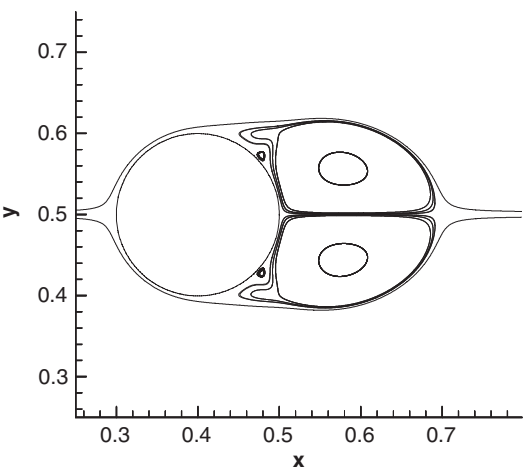

Figure 8. Impulsively started cylinder, $Re = 550$, $t_s = 3.0$, instantaneous streamlines.

$u_{\text{B}} = 2\pi f_e A \cos[2\pi f_e(t - t_s) + 0.5\pi]$. The initial condition at $t = t_s$ is the solution for the flow over a stationary cylinder with its centre at $x_{\text{c}} = 0.24d$.

Figure 9 shows the vorticity contours in sequence over two oscillation periods ($2T$) of the cylinder. The vortex shedding pattern of the stationary case (Figure 6) is modified by the oscillation of the cylinder. For the chosen oscillation frequency, the vortex-shedding pattern is in anti-symmetrical A-III mode, according to the experimental observation of Ongoren and

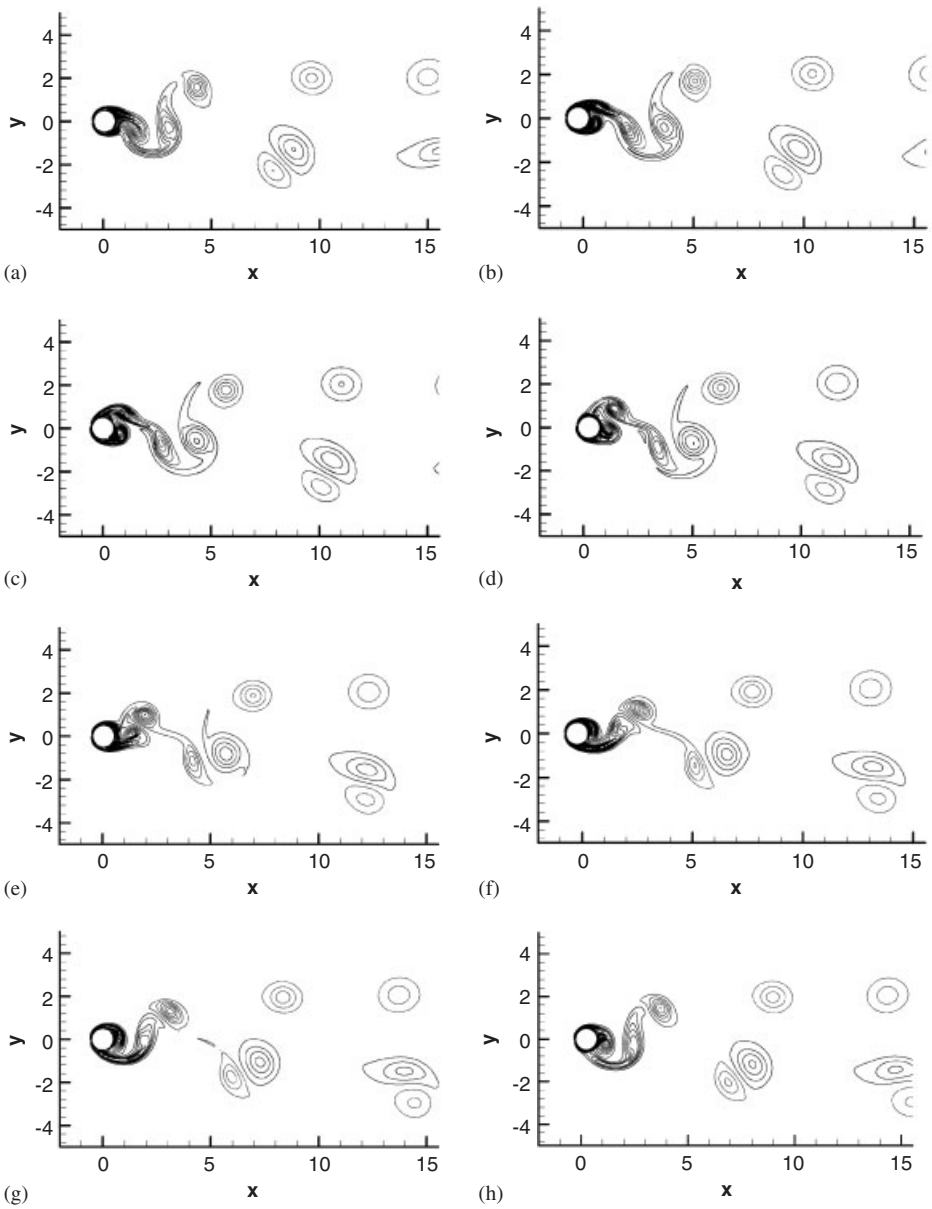

Figure 9. Circular cylinder oscillating in parallel to the free stream, $Re = 200$, oscillation frequency $f_e = 1.5St$, oscillation amplitude $A = 0.24d$: (a) $t = 6/25T$; (b) $t = 13/25T$; (c) $t = 19/25T$; (d) $t = 25/25T$; (e) $t = 31/25T$; (f) $t = 38/25T$; (g) $t = 44/25T$; and (h) $t = 50/25T$.

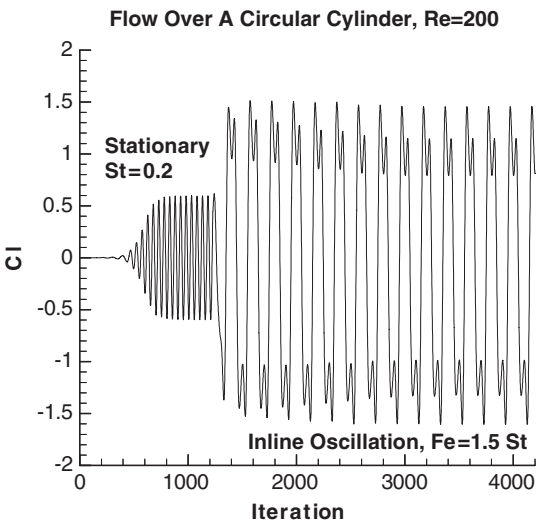

Figure 10. Record of lift coefficient, $Re = 200$, cylinder stationary before 1225 iterations.

Rockwell [16]. There are three vortices being shed from the cylinder and the whole shedding process takes two oscillation periods to complete. In Figures 9(g), (h), (a)–(d), two clockwise vortices shed from the top of the cylinder, while in Figures 9(c)–(g) one counter-clockwise vortex shed from the bottom of the cylinder. One of the clockwise vortices (the one shed in Figures 9(c) and (d)) moves downstream along a path above the cylinder, while the other clockwise vortex (the one shed in Figures 9(h), (a) and (b)) pairs with the counter-clockwise one to form a vortex pair, moving downstream in a lower position. This vortex street pattern is in good agreement with the experimental observation of Ongoren and Rockwell [16].

Figure 10 shows the record of the lift coefficient. For the first 1225 iterations in Figure 10, the cylinder is stationary with its centre at $x_c = 0.24d$. Then the inline oscillation starts at t_s with a new time increment that takes about 100 iterations to complete one period of oscillation. Note that the record in Figure 10 is smooth before and after the transition from a stationary cylinder to an oscillating cylinder. The FFT analysis for the record after t_s gives a major peak at f_e and some minor peaks at the multiples of $0.5f_e$. This example has validated the capability of the present method to handle large body movement.

CONCLUSIONS

A simple and effective immersed boundary method has been developed and validated for incompressible flows. The basic idea is to view the domain inside the solid body as being occupied by the same fluid as outside with a prescribed divergence-free velocity distribution. The flow solver is a second-order accurate implicit fractional-step method on unstructured Cartesian meshes. The convection fluxes are calculated by a MUSCL-type upwind scheme and the viscous fluxes by a central difference scheme. The volume of body (VOB) function is used as a natural parameter that relates the flow solution outside the body to the known velocity

distribution inside the body. The velocity at the interface cell is a volume-averaged mixture of the known body velocity and the velocity estimated by the conservation equations. The same pressure Poisson equation is used for the entire computational domain without distinguishing the cell type. A background dissipation proportional to the forth derivative of pressure is added to minimize the pressure oscillation around the body surface. Implicit multigrid methods are developed to solve the difference equations for both pressure and velocity. The computations of driven cavity flows and flows over a circular cylinder show good comparisons with the work of others. Finally, the wake flow of an impulsively-started cylinder and the vortex shedding patter over a cylinder oscillating inline with the free stream are computed to validate the capability of the present method to treat moving bodies.

ACKNOWLEDGEMENTS

This work is funded by National Science Council under the grants NSC91-2212-E006-104 and NSC92-2212-E006-105. The support is highly appreciated.

REFERENCES

1. Peskin CS. The immersed boundary method. *Acta Numerica* 2002; 1–39.
2. Goldstein D, Handler R, Sirovich L. Modeling a no-slip flow boundary with an external force field. *Journal of Computational Physics* 1993; **105**:354–366.
3. Saiki EM, Biringen S. Numerical simulation of a cylinder in uniform flow: application of a virtual boundary method. *Journal of Computational Physics* 1996; **123**:450–465.
4. Fadlun EA, Verzicco R, Orlandi P, Mohd-Yusof J. Combined immersed-boundary finite-difference methods for three-dimensional complex flow simulations. *Journal of Computational Physics* 2000; **161**:35–60.
5. Kim J, Kim D, Choi H. An immersed-boundary finite-volume method for simulations of flow in complex geometries. *Journal of Computational Physics* 2001; **171**:132–150.
6. Baaijens Frank PT. A fictitious domain/mortar element method for fluid-structure interaction. *International Journal for Numerical Methods in Fluids* 2001; **35**:743–761.
7. Ye T, Mittal R, Udaykumar HS, Shyy W. An accurate Cartesian grid method for viscous incompressible flows with complex immersed boundaries. *Journal of Computational Physics* 1999; **156**:209–240.
8. Xiao F. A computational model for suspended large rigid bodies in 3D unsteady viscous flows. *Journal of Computational Physics* 1999; **155**:348–379.
9. Kajishima T, Takiguchi S. Interaction between particle clusters and particle-induced turbulence. *International Journal of Heat and Fluid Flow* 2002; **23**:639–646.
10. Rhie CM, Chow WL. A numerical study of the turbulent flow past an airfoil with trailing edge separation. *AIAA Journal* 1982; **21**:1525–1532
11. Ethier CR, Steinman DA. Exact fully 3D Navier–Stokes solutions for benchmarking. *International Journal for Numerical Methods in Fluids* 1994; **19**:369–375.
12. Ghia U, Ghia KN, Shin CT. High-Re solutions for incompressible flow using the Navier–Stokes equations and a multigrid method. *Journal of Computational Physics* 1982; **48**:387–411.
13. Fornberg B. A numerical study of steady viscous flow past a circular cylinder. *Journal of Fluid Mechanics* 1980; **98**:819–855.
14. Kiris C, Kwak D. Numerical solution of incompressible Navier–Stokes equations using a fractional-step approach. *Computers and Fluids* 2001; **30**:829–851.
15. Bouard R, Coutanceau M. The early stage of development of the wake behind an impulsively started cylinder for $40 < Re < 10^4$. *Journal of Fluid Mechanics* 1980; **101**:583–607.
16. Ongoren A, Rockwell D. Flow structure from an oscillating cylinder, Part 2. Mode competition in the near wake. *Journal of Fluid Mechanics* 1988; **191**:225–245.

